

Stopped and stationary light at the single-photon level inside a hollow-core fiber

Thorsten Peters, Ta-Pang Wang, Antje Neumann, Lachezar S. Simeonov,* and Thomas Halfmann
Institut für Angewandte Physik, Technische Universität Darmstadt, Hochschulstrasse 6, 64289 Darmstadt, Germany

(Dated: November 4, 2021)

An experimental platform operating at the level of individual quanta and providing strong light-matter coupling is a key requirement for quantum information processing. We report on narrowband light storage and retrieval as well as stationary light, based on electromagnetically induced transparency, for weak coherent light pulses down to the single-photon level with a signal-to-noise ratio of 59. The experiments were carried out with laser-cooled atoms loaded into a hollow-core photonic crystal fiber to provide strong light-matter coupling, thereby demonstrating the prospects for future quantum networks of such a platform.

I. INTRODUCTION

Optical quantum information processing [1] requires generation, processing and detection of individual photons. Huge efforts have been dedicated to building high-brightness single-photon sources [2], implementing efficient quantum memories [3], and developing schemes to provide strong light-matter coupling, allowing for interactions between individual photons [4].

A powerful approach towards high memory efficiency [5] and interaction between photons is based on electromagnetically induced transparency (EIT) with atomic ensembles [6]. EIT permits reversible group velocity control, e.g., for light storage and retrieval (LSR) [6] and stationary light pulses (SLPs) [7], as well as interactions between light fields via a Kerr-type nonlinearity [8–10]. SLPs are of particular interest due to their potential for nonlinear optics at the few-photon level [10–12]. Although an EIT-driven memory and SLPs with non-classical quantum states were demonstrated in free-space cold atomic ensembles [13–15], demonstrations of nonlinear optical interactions were so far restricted to classical light pulses of large average photon number \bar{n} [16]. Large nonlinearities require that two photons interact with the same atom simultaneously, which can be quantified by the optical depth per atom $d_{opt}^* = \sigma_0/\pi w_0^2$ [4], where σ_0 is the atomic absorption cross-section and w_0 is the waist of the Gaussian beam. This requires very tight focusing of the laser beams and thus results in small interaction volumes in free-space setups and, hence, small optical depths $d_{opt} = \sigma_0 n L$, where n is the atomic number density and L is roughly given by the Rayleigh length. As the coupling strength of light to atomic ensembles is proportional to the optical depth d_{opt} , which also determines the LSR efficiency [17], experimental setups are required that provide both large d_{opt} and d_{opt}^* . Therefore, in recent years there have been efforts to couple atomic ensembles to waveguides such as hollow-core photonic crystal fibers (HCPCFs) [18–20], tapered optical nanofibers [21], and nanoscale photonic crystals [22], which allow

for tight transversal confinement of light and atoms over macroscopic distances.

Operation at the quantum level requires strong suppression of the background (caused mainly by the strong control beam in EIT). However, spatial filtering as in free-space setups cannot be applied due to the 1D geometry of the waveguides. So far, LSR in waveguide-coupled atomic ensembles at the single-photon level (SPL) has been demonstrated for broadband photons employing a Raman protocol and room-temperature atoms [23] and narrowband photons employing EIT and cold atoms coupled to optical nanofibers [24, 25]. The latter demonstrations reported $d_{opt} \lesssim 6$ and a LSR efficiency of $\eta_{LSR} \lesssim 10\%$ (where η_{LSR} is defined as the ratio of retrieved to input pulse area). Larger η_{LSR} and the ability to generate SLPs is expected in HCPCFs filled with cold atoms due to the larger $d_{opt} \lesssim 1000$ in such setups [26]. However, background suppression by polarization filtering is further hampered in HCPCFs by strong birefringence [27, 28] stemming from structural features much smaller than the periodicity of the HCPCF cladding structure [29]. Further difficulties arise also due to the correspondingly larger control beam power $P_c \propto \sqrt{d_{opt}}$ required for the same EIT transmission window width $\Delta\omega_{EIT} = \Omega_c^2/\Gamma\sqrt{d_{opt}}$ [30], where Γ is the excited state decay rate and Ω_c is the control Rabi frequency.

Here we demonstrate the storage and retrieval of weak narrowband coherent light pulses, and the creation of SLPs down to the SPL in an ensemble of laser-cooled atoms inside a HCPCF. Compared to our previous work [31], we carefully characterized the birefringence of our HCPCF to overcome its detrimental effects, enabling efficient polarization filtering. Also, we apply a fine structure transition with larger transition moment for the control, enabling operation at lower power, as well as reduced off-resonant absorption and inhomogeneous ac Stark shifts due to fewer excited hyperfine states at larger detuning. This leads to an increased efficiency and improved signal-to-noise (SNR) ratio by roughly 20 dB and thus enables operation at the SPL.

* Now at: Department of Physics, Saint Kliment Ohridski University of Sofia, 5 James Bourchier Boulevard, 1164 Sofia, Bulgaria

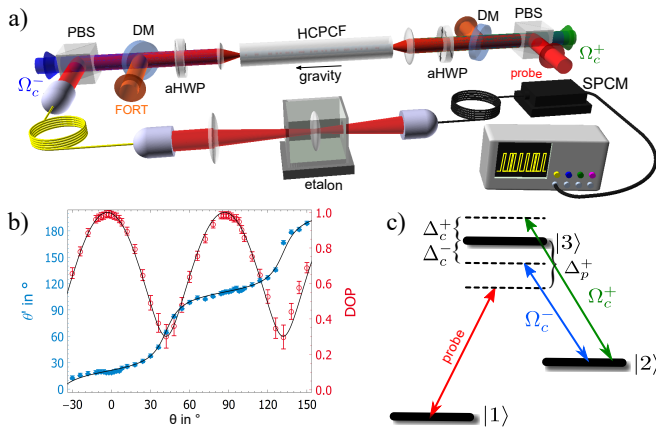


FIG. 1. a) Simplified experimental setup. PBS: polarizing beam splitter, DM: dichroic mirror, SPCM: single-photon counting module. b) Measured DOP and output polarization direction θ' after the HCPCF (symbols) as a function of linear input polarization direction θ . The black lines are simulations based on the theory in the SM. c) Level scheme for EIT-based LSR and SPLs. $|1\rangle, |2\rangle = 5^2S_{1/2}$, $F = 1, 2$, and $|3\rangle = 5^2P_{1/2}$, $F' = 1$.

II. EXPERIMENTAL SETUP

We implement the experiment with cold ^{87}Rb atoms, loaded from a magneto-optical trap (MOT) into a HCPCF (NKT Photonics HC-800-02), involving a far off-resonant optical trap (FORT) to guide the atoms inside the fiber and prevent collisions with the room-temperature fiber wall [26]. The probe laser is locked with an offset of 76 MHz to the corresponding transition via bichromatic saturation absorption spectroscopy [32]. The control laser is phase-locked to the probe yielding a two-photon linewidth of ~ 8 kHz [31]. Acousto-optic modulators (AOMs) shift the frequencies to the required detuning. Probe and control fields have orthogonal linear polarizations. The FORT laser system uses two superimposed orthogonally-polarized laser diode beams at 820 nm. With a trapping power of 110 mW inside the HCPCF, we obtain a trap depth of around 4 mK. To adjust the linear polarizations of all fields inside the HCPCF at wavelengths of 780 nm, 795 nm, and 820 nm, we use achromatic half-wave plates (aHWP) [see Fig. 1(a)]. For more experimental details see [26, 31] and the Appendix.

III. EXPERIMENTAL RESULTS

Suppression of the strong control beam Due to the HCPCF's strong birefringence [27, 28], we previously could attenuate the strong control beam only by 35 dB using a combination of two PBSs behind the fiber. This lead to a total suppression of 74 dB (64 dB relative to the probe beam) [31] and limited the probe pulses to $\bar{n} \gtrsim 70$ photons. We therefore conducted a thorough

study of the birefringence properties of our fiber by analyzing the degree of polarization (DOP) at the output of our HCPCF as a function of linear input polarization direction θ . Fitting the DOP and orientation θ' of the major polarization axis at the output [see Fig. 1(b)] to theoretical predictions including linear and circular birefringence (see Appendix), we find that our fiber is predominantly linearly birefringent (probably due to the elliptical core) with only a small admixture of circular birefringence. The resulting polarization beat length is $L_b = 8.0(8)$ mm, i.e., similar to standard polarization-maintaining fibers, with a maximum achievable DOP of $0.9925(10)$. Matching the input polarizations to the optical axis of the HCPCF thus enables attenuation of the control beam by up to 86 dB, i.e., a 12 dB improvement, while using only a single PBS after the HCPCF. The overall transmission of the probe beam increases slightly to $0.13(1)$. By switching to the D_1 line with a larger transition strength for the control field, its background can be reduced by another 8 dB while maintaining a large Rabi frequency. This yields a total background suppression improvement of 20 dB and enables experiments at the SPL.

Light Storage & Retrieval of Coherent Light pulses We now turn to LSR with the coupling scheme shown in Fig. 1(c), where only the forward control field Ω_c^+ is switched on, while the backward control field $\Omega_c^- \equiv 0$. Details on the LSR pulse sequence can be found in the Appendix. EIT creates dark-state polaritons (DSPs) with a moving photonic and a non-moving atomic coherence between states $|1\rangle$ and $|2\rangle$ [33]. The group velocity of the DSPs can be controlled by Ω_c^+ . Ramping Ω_c^+ adiabatically down to zero maps the photonic DSP component onto the non-moving atomic component. By ramping the control field back up, the coherence is retrieved into a moving light pulse [30]. We modulate the control field with an AOM to produce storage periods of variable duration τ_{LSR} . The measured transmissions for $\tau_{LSR} = 200$ ns and $\tau_{LSR} = 500$ ns are shown in Fig. 2 in dark blue and red, respectively, for Gaussian probe pulses of $1/e$ full width $\tau_p = 150(2)$ ns and $\bar{n} = 17(3)$ photons per input pulse. For reference we show the input probe pulse without atoms loaded into the HCPCF and a slow light pulse with constant control Rabi frequency in black and gray, respectively. The solid lines represent Gaussian least-squares fits to the experimental data. From these fits we obtain a LSR efficiency of $\eta_{LSR} = [0.36(4); 0.25(3)]$ for storage times of $\tau_{LSR} = (200; 500)$ ns, respectively. This is significantly larger compared to related work [24, 25], due to the higher d_{opt} in our experiment. By plotting the retrieval efficiency vs. storage time and fitting the data with an exponential decay we obtain a decay rate of $\gamma_{21} = 0.26(2)\Gamma$. In the same figure we also plot the results for LSR with coherent input pulses containing $\bar{n} = 1.1(2)$ photons (light blue and red). There is very good agreement between the pulses at the SPL and those with higher photon numbers.

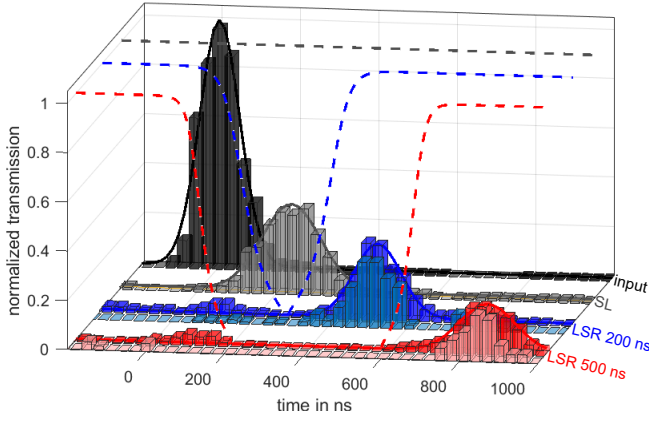


FIG. 2. Measured normalized transmission (bars) through the HCPCF vs. time for input pulses (black) containing $\bar{n} = 17(3)$ photons, slow light (SL) (gray), and LSR for $\tau_{LSR} = 200$ ns (blue) and $\tau_{LSR} = 500$ ns (red). The light blue and red bars correspond to $\bar{n} = 1.1(2)$ photons per input probe pulse. The solid colored lines are Gaussian least-squares fits to the corresponding experimental data. The dashed colored lines schematically show the corresponding timing of $\Omega_c^+(t)$. All experimental data are scaled with respect to the fit amplitude of the input pulse. The parameters are: $\Omega_c = 3.6(2)\Gamma$, $d_{opt} = 109(10)$. The data was averaged over 1500 runs.

Stationary Light Pulses. LSR allows for the stopping of light pulses. However, as the photons are converted into atomic coherences, no light is inside the medium during the storage period, prohibiting nonlinear optical interactions. In order to reduce the group velocity of the DSPs to zero while maintaining a photonic component (i.e., a light pulse), a second counter-propagating control beam of Rabi frequency Ω_c^- can be added while the probe pulse is inside the medium [34]. This creates a SLP with a quasi-stationary envelope which allows for nonlinear optical interactions. Details on the SLP sequence can be found in the Appendix. In order to keep the effective group velocity $v_{gr} \propto \Omega_0^2$ with $\Omega_0^2 = (\Omega_c^+)^2 + (\Omega_c^-)^2$ [35] of the DSPs almost constant during the whole experiment, we reduce Ω_c^+ during the SLP period τ_{SLP} , when Ω_c^- is on. This allows for a better comparison with SL data, where $\Omega_c^- \equiv 0$. Without keeping Ω_0^2 constant, the effective DSP group velocity would be more than doubled during τ_{SLP} . In Fig. 3(a) we compare the results of three different conditions. The input pulse (black) is scaled down by a factor of 0.2 for better comparison. The probe signal for times $t \lesssim 150$ ns apparent in the gray, blue and magenta data sets corresponds to the rising edge of the probe pulses which have already left the medium before the SLP period starts. When $\Omega_c^- \equiv 0$ and Ω_c^+ is modulated according to the gray dashed line, we observe a spread-out probe pulse due to the much reduced group velocity during $\Delta t_{SLP} = 150$ ns $\lesssim t \lesssim 650$ ns (gray bars). When the backward control field (magenta dotted line) is much stronger than the forward control (magenta dashed line) during Δt_{SLP} , with $\Omega_c^-/\Omega_c^+ = 1.84$, we ob-

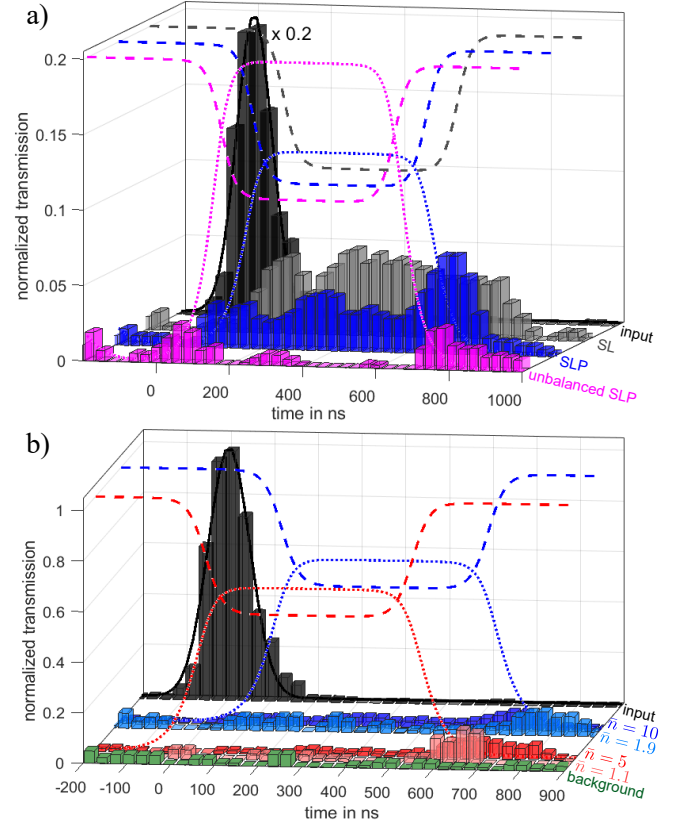


FIG. 3. Measured normalized transmission (bars) through the HCPCF vs. time. The solid black lines are least-squares fits to the Gaussian input pulse [black; scaled down by a factor of 0.2 in (a)] without atoms inside the HCPCF. All experimental data is scaled with respect to the fit amplitude of the input pulse. a) SL (gray) with a modulated Ω_c^+ (gray dashed); SLP (blue) for Ω_c^- (blue dashed) and Ω_c^+ (blue dotted) slightly unbalanced during τ_{SLP} ; backward propagating quasi-SLP (magenta) for Ω_c^+ (magenta dashed) and Ω_c^- (magenta dotted) strongly unbalanced during τ_{SLP} . b) SLPs for $\bar{n} = 10(2)$ [blue; same data as in (a)] and $\bar{n} = 1.9(4)$ photons per pulse (light blue). Other experimental run for $\bar{n} = 5(1)$ (red) and $\bar{n} = 1.1(2)$ photons per pulse (light red) where the control timing was shifted by -115 ns compared to the blue data. The background signal, when the input probe pulse is blocked, is shown in green. The parameters are: $d_{opt} \sim 80(5)$ [except for the red data where $d_{opt} \sim 70(5)$], $\Omega_c^+ = 3.5(2)\Gamma$ (gray, blue, magenta dashed), $\Omega_c^- = [2.3(2); 3.5(2)]\Gamma$ [(blue; magenta) dotted], $\Omega_c^+ = 3.0(2)\Gamma$ (red dashed), $\Omega_c^+ = 2.4(2)\Gamma$ (red dotted) $\Delta_p^+ = \Delta_c^+ = 0$, $\Delta_c^- = +2.5\Gamma$, $\tau_{SLP} = 500$ ns.

serve basically no transmission during Δt_{SLP} and only a very small retrieved probe signal after the backward control is switched off (magenta bars). This small signal in addition is delayed with respect to the switch-off time of the backward control field. The delayed read-out can be well-explained by considering the SLP group velocity $v_{gr}^{SLP} = v_{gr} \cos 2\phi$ with $\tan^2 \phi = |\Omega_c^-|^2/|\Omega_c^+|^2$ [35]. For $\Omega_c^-/\Omega_c^+ = 1.84$ the SLP propagates backward at around $-0.55 \times v_{gr}$ during Δt_{SLP} and thus exits the medium at later times during the retrieval in the forward direction.

In contrast, when Ω_c^+ and Ω_c^- are nearly balanced for optimum SLP conditions (blue dashed and dotted lines), there is some leakage of light during τ_{SLP} [but reduced compared to SL (gray bars)] and a significantly larger retrieved probe pulse area after the backward control is switched off (blue bars). This is the typical signature of a SLP having a non-vanishing intensity at the edges of the medium and therefore showing leakage [15, 31, 34, 36]. By calculating the retrieved pulse area after Δt_{SLP} we obtain a SLP retrieval efficiency of $\eta_{SLP} = 0.14(2)$, i.e., a five-fold improvement compared to our previous work [31]. Therefore, η_{SLP} is now of the same order as the corresponding η_{LSR} (see above). The experimental data shown here are a selection of experimental runs where we varied the backward control Rabi frequency during τ_{SLP} between $0\Gamma \leq \Omega_c^- \leq 3.5\Gamma$. We obtained the largest SLP retrieval efficiency when $\Omega_c^- \sim 1.2 \times \Omega_c^+$ during Δt_{SLP} . We already discussed this in [31] as the result of the phase-mismatch present for the generated backward probe field in our 1D system. By choosing a larger Ω_c^- , this phase-mismatch can be compensated to some extent. In Fig. 3(b) we compare the results for weak coherent input pulses containing $\bar{n} = 10(2)$ (dark blue) to $\bar{n} = 1.9(4)$ photons (light blue) and $\bar{n} = 5(1)$ (dark red) to $\bar{n} = 1.1(2)$ photons (light red) from a different experimental run. The background noise is shown for reference in green, reaching a level of 1.1×10^4 photons per second and corresponding to a input SNR of roughly 59. The efficiencies η_{SLP} for higher and lower \bar{n} agree with each other within 3% for each experimental run. This data clearly demonstrates the potential of a HCPCF loaded with laser-cooled atoms as a suitable platform for EIT-based quantum information processing.

Discussion. Although the demonstrated LSR and SLP retrieval efficiencies are sufficient to reliably detect pulses at the SPL, we might expect $\eta_{LSR} \gtrsim 0.85$ for our $d_{opt} \sim 100$ [17]. To investigate this limited efficiency, we studied EIT spectra and compared the measured data to a numerical simulation including the radially varying control intensity and atomic density [31]. Detrimental effects due to (inhomogeneous) ac Stark shifts are much reduced at the D_1 compared to the D_2 line. However, the measured peak transmission is lower than expected from the simulation. For small EIT window widths, where typically LSR and SLP experiments are performed, this larger absorption simply reduces efficiencies. For larger window widths, however, this reduced transmission can be turned into a single low-transmission resonance within $\Delta\omega_{EIT}$, which we did not observe on the D_2 line for the same transition [31]. This issue is currently still under investigation and, if solved, will lead to even higher storage efficiencies.

IV. SUMMARY

In summary, we demonstrated EIT-based LSR and SLPs for weak coherent light pulses containing as low as

$\bar{n} = 1.1(2)$ photons per pulse, implemented in a medium of cold atoms inside a HCPCF. We observed a LSR and SLP efficiency of up to 0.36(4) and 0.14(2), respectively, at the SPL with a SNR of 59. This was enabled, amongst others, by a careful characterization and use of a mainly linearly birefringent HCPCF, resulting in efficient suppression of the strong control beam. With $d_{opt} \sim 100$ and $d_{opt}^* \sim 0.0017$, our results demonstrate the potential of HCPCFs loaded with laser-cooled atoms as a suitable experimental platform operating at the quantum level, while simultaneously providing strong light-matter coupling.

FUNDING INFORMATION

European Union's Horizon 2020 research and innovation programme under the Marie Skłodowska-Curie grant agreement No. 765075.

ACKNOWLEDGMENTS

The authors thank H.R. Hamed, G. Birkl and M. Fleischhauer for discussions, F. Blatt for assistance with measurements, and the group of T. Walther for providing us with a home-made ultra-low noise laser diode driver with high modulation bandwidth.

Appendix A: Birefringence characterization of the HCPCF

1. Theoretical analysis

In analogy to common glass fibers, the HCPCF used in our experiment, is supposed to be highly birefringent due to the geometric asymmetry of the elliptic core and the additional symmetry breaking structural elements inside the cladding zone next to the core [27, 28]. To model the birefringence of the fiber, we assume an in general elliptical birefringence. The initial light field is linearly polarized with real amplitude \mathcal{E}_0 and input orientation θ , oscillating in the x - y -plane

$$\vec{\mathcal{E}}(z=0) \equiv \vec{\mathcal{E}}_0 = \begin{pmatrix} \mathcal{E}_{0,x} \\ \mathcal{E}_{0,y} \end{pmatrix} = \begin{pmatrix} \mathcal{E}_0 \cos \theta \\ \mathcal{E}_0 \sin \theta \end{pmatrix}. \quad (\text{A1})$$

We use the Jones formalism with Jones matrix J to describe the effect of the birefringent fiber on the electromagnetic field

$$\vec{E}(z, t) = J\vec{E}(z=0, t), \quad \vec{E}(z, t) = \text{Re} \left[\vec{\mathcal{E}}(z) e^{-i\omega t} \right], \quad (\text{A2})$$

where we consider only the physically relevant real part. The Jones matrix J for elliptical birefringence reads [37,

38]

$$J = \begin{pmatrix} \cos \frac{\phi}{2} - i \sin \frac{\phi}{2} \cos \chi & -\sin \frac{\phi}{2} \sin \chi \\ \sin \frac{\phi}{2} \sin \chi & \cos \frac{\phi}{2} + i \sin \frac{\phi}{2} \cos \chi \end{pmatrix}, \quad (\text{A3})$$

with ϕ defining the linear and χ the circular birefringence.

It is worth mentioning, that (A3) provides a fixed main axis. However, in the case of a HCPCF this theoretical main axis can differ from the geometrical main axis of the elliptical core [see Fig. 4(a)]. This can be possibly due to a change of its orientation over the fiber length, e.g., by an intrinsic torsion. We take this variation into account by adjusting the input angle $\tilde{\theta} = \theta - \beta$ with the orientation of the theoretical fixed main axis in relation to the horizontal axis β , visualized in Fig. 4 (a).

To characterize the birefringence of the HCPCF the orientation of the output field's main axis can be calculated with

$$\theta' = \text{Re} \left[\arctan \left(\frac{\mathcal{E}_y(\tilde{\theta}, \phi, \chi)}{\mathcal{E}_x(\tilde{\theta}, \phi, \chi)} \right) \right] + \beta \quad (\text{A4})$$

as well as the degree of linear polarization (DOP). In general this is given by the relation of the field intensity's maximum and minimum

$$\text{DOP} = \frac{I_{\max} - I_{\min}}{I_{\max} + I_{\min}}, \quad (\text{A5})$$

with $\text{DOP} = 1$ for completely linear polarized light.

We would like to express DOP as a function of θ . Therefore, we first calculate the general form of $\vec{E}(z, t)$. By inserting (A1) and (A3) into (A2) we get

$$E_x(z, t) = A \cos(-\omega t) + B \sin(-\omega t), \quad (\text{A6})$$

$$E_y(z, t) = C \cos(-\omega t) + D \sin(-\omega t), \quad (\text{A7})$$

with

$$A = \mathcal{E}_0 \left[\cos \tilde{\theta} \cos \frac{\phi}{2} - \sin \tilde{\theta} \sin \chi \sin \frac{\phi}{2} \right], \quad (\text{A8})$$

$$B = -\mathcal{E}_0 \cos \chi \sin \frac{\phi}{2} \cos \tilde{\theta}, \quad (\text{A9})$$

$$C = \mathcal{E}_0 \left[\cos \tilde{\theta} \sin \frac{\phi}{2} \sin \chi + \sin \tilde{\theta} \cos \frac{\phi}{2} \right], \quad (\text{A10})$$

$$D = \mathcal{E}_0 \sin \tilde{\theta} \cos \chi \sin \frac{\phi}{2}. \quad (\text{A11})$$

$\vec{E}(z, t)$ fulfills the equation of a rotated ellipse

$$\frac{C^2 + D^2}{\Delta^2} E_x^2 + \frac{A^2 + B^2}{\Delta^2} E_y^2 - 2 \frac{AC + BD}{\Delta^2} E_x E_y = 1, \quad (\text{A12})$$

with $\Delta = AD - BC$. To identify I_{\max} and I_{\min} we have to bring (A12) to the normal form $r_1 E_x^2 + r_2 E_y^2 = 1$, because then

$$\text{DOP} = \frac{r_2 - r_1}{r_2 + r_1} = \sqrt{1 - \frac{4(AD - BC)^2}{A^2 + B^2 + C^2 + D^2}}. \quad (\text{A13})$$

With $A^2 + B^2 + C^2 + D^2 = \mathcal{E}_0^2$ we finally obtain

$$\text{DOP} = \sqrt{1 - 4 \cos^2 \chi \sin^2 \frac{\phi}{2} \left(\sin 2\tilde{\theta} \cos \frac{\phi}{2} + \cos 2\tilde{\theta} \sin \frac{\phi}{2} \sin \chi \right)^2}. \quad (\text{A14})$$

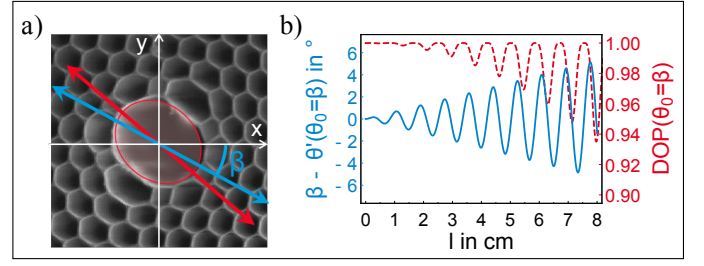


FIG. 4. (a) Scanning electron image of the central region of our HCPCF. The orientation of the optical axis β (blue) can differ from the main axis of the elliptical core (red). (b) Calculated DOP as a function of fiber length l and absolute rotation of the input polarization using the same parameters as in (b). For a length of $l \leq 3.5$ cm and an input angle $\theta = \beta$ the polarization can be maintained sufficiently well, if we assume $\text{DOP} \geq 0.99$ and $\Delta\theta \leq 2^\circ$.

We can use this theoretical model for the DOP in (A14) as well as the orientation of the output field in (A4) to fit the experimental data and obtain the linear and circular birefringences.

2. Experimental analysis

Starting with an almost perfectly linear-polarized input field [$\text{DOP} = 0.999985(5)$], we measure θ' and DOP depending on the input orientation θ , adjusted by an aHWP, which impairs the input polarization to $\text{DOP} \geq 0.9984$. The spatial intensity distribution of the output field is analyzed with a Glan-Thompson polarizer and normalized to the input power, resulting in $P(\vartheta)/P_0 = b + a \sin(\vartheta)$. Then the DOP is given by $\text{DOP} = a/b$. The orientation θ' corresponds to the position of the maxima, respectively, the minima plus 90° , as the determination of the latter is more precise. Due to the high asymmetry of our fiber core it is important to make sure that only the approximately Gaussian-shaped mode transmitted through the core is analyzed. Higher-order modes that can propagate through the cladding zone drastically reduce the DOP.

The results for a nearly untwisted fiber (NKT Photonics HC-800-02) of length $l_F \approx 22$ cm are depicted in Fig. 1(b). Note that in general $\phi = \phi + 2n\pi$, $n \in \mathbb{Z}$. However with the wavelength-sweeping technique [39], the exact value of ϕ can be calculated. Hence, we require two measurements of the DOP for different wavelengths $\lambda_1 \neq \lambda_2$ with $\text{DOP}(\theta, \lambda_1) \approx \text{DOP}(\theta, \lambda_2)$. More details can be found in [39]. Unfortunately, the latter condition is not fulfilled for a fiber length of $l_F \approx 22$ cm. We therefore used a shorter fiber of length $l_F \approx 2$ cm to determine ϕ . We then extrapolated $\phi(l_F \approx 22 \text{ cm}) \approx \frac{22 \text{ cm}}{2 \text{ cm}} \phi(l_F \approx 2 \text{ cm}) = 11 \cdot 15.20(6) = 167(1)$. This value is then used as a starting point to fit the theoretical curves from (A14) and (A4) to the experimental data shown in Fig. 1(b) of the main document while slightly changing $\phi = 167$ by $\pm\pi$. Here, the importance of the fit of $\theta'(\theta)$ becomes

apparent. Only both fits together identify one unique ϕ in the given range. For our fiber we obtain the values

$$\phi = 164.84(5), \quad \chi = 0.50(5), \quad \beta = 0.15(2).$$

The degree of linear polarization obviously depends strongly on the input polarization orientation. The maximum $\text{DOP}_{\text{max}} = 0.9925(10)$ for an input orientation $\theta = -2^\circ \pm 1^\circ$ and $\theta' = 19^\circ \pm 1^\circ$ shows, that for certain input orientations, the HCPCF can almost maintain the input DOP. In addition, for an input orientation along the theoretical optical axis, we may expect to achieve the best conservation of the input orientation. However, for $\theta = \beta = 8.6^\circ \pm 1.1^\circ$ we get $\text{DOP} = 0.93$ and $\theta' = 24^\circ \pm 2^\circ$, because both depend on the fiber length. In Fig. 4 (b) the deviation between output and input polarization direction for $\theta = \beta$ and the DOP is depicted as a function of the fiber length. For $l \lesssim 3.5$ cm indeed we can reach $\text{DOP} \geq 0.99$ and the change of the orientation $\Delta\theta \leq 2^\circ$ is very small. For fiber lengths $l \gtrsim 3.5$ cm a good DOP can be maintained by choosing a different input polarization orientation $\theta \neq \beta$, which is necessary due to the small elliptical birefringence of our fiber. Comparing the polarization beat length $L_b = 2\pi l_F / \phi \approx 0.80(8)$ cm, to common glass fibers with typical L_b of several meters and polarization maintaining fibers with $L_b \lesssim 1 \dots 3$ mm, in fact, our HCPCF can be assigned rather to the latter kind.

We note that the dominant linear birefringence of our fiber is probably due to the elliptical core with an aspect ratio of around 1.3 [29]. Without this large asymmetry, the birefringence properties might be more complex [28] and we would not be able to maintain the linear polarizations of the laser beams as they propagate through the HCPCF. This would inhibit efficient polarization filtering at the output and prevent experiments at the SPL.

Appendix B: Experimental Sequences

The schematic time sequence for loading the HCPCF with atoms is shown in Fig 5(a). The MOT is loaded for 990 ms with a Gaussian-shaped repumper beam in addition to the dark funnel repumper [26] to increase the number of atoms in the MOT. After the MOT loading phase the MOT repumper is switched off by a mechanical shutter and only the dark funnel repumper is left for increasing the density of atoms above the HCPCF. Simultaneously, the current of the quadrupole coils is doubled for compression of the cloud and the magnetic offset field in the z -direction (along the fiber axis) is changed to move the atoms towards the fiber tip. During the 40 ms long shift and compression and the 20 ms long HCPCF loading phases, the trapping detuning is ramped from -2.5Γ to -5Γ for sub-Doppler cooling above the HCPCF to increase the loading efficiency. During the HCPCF loading phase the atoms are held above the HCPCF where the FORT potential is strong enough to guide the atoms into the fiber. A depumper beam, tuned 133 MHz to the blue

side of the transition ${}^2S_{1/2}, F = 2 \leftrightarrow {}^2P_{3/2}, F' = 2$, to account for the ac Stark shift by the FORT, is continuously on and serves to confine the atoms inside the dark funnel in $F = 1$ for enhancing the density near the fiber tip. After loading the HCPCF is finished at 1050 ms and

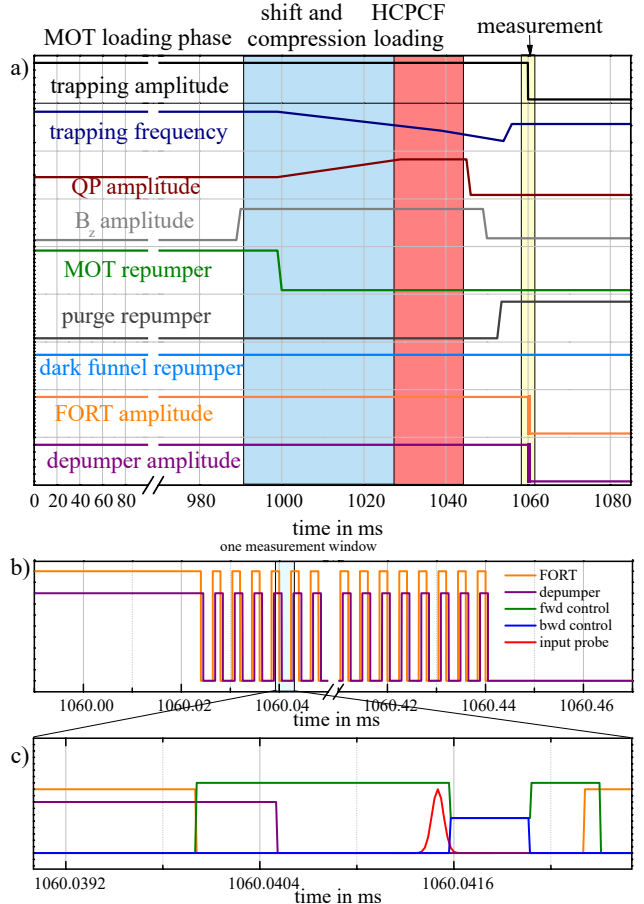


FIG. 5. a) Time sequences of laser and magnetic fields for loading the HCPCF with atoms. QP: quadrupole field of the MOT coils; B_z : magnetic offset field in the vertical direction that determines the zero point of the magnetic field and thereby shifts the atom cloud above the HCPCF. b) Sequence of the FORT and depumper for the SL/LSR/SLP experiments. c) Sequence of the laser fields used for SL/LSR/SLP measurements.

another 10 ms period for letting the quadrupole field decay, experimental runs of SL, LSR or SLPs start. The FORT (and the depumper) are rapidly switched on and off at a frequency of 250 kHz according to Fig. 5(b). This eliminates ac Stark shifts by the FORT during the measurement windows of $2.5 \mu\text{s}$ duration, but is still short enough to not lose a significant amount of atoms during this free expansion. Up to 50 measurements can be done with the same atoms loaded into the fiber, before losses became noticeable. In each time slot when the FORT is off, SL/LSR/SLP measurements [see Fig.5(c)] are performed. The first 4 time slots are used to prepare the population in $F = 1$ by the control beam. We do not try to prepare the population in a single Zeeman level. Then,

Gaussian probe pulses of $\tau_p = 150(2)$ ns $1/e$ full width are sent into the HCPCF in the next 25 time slots. Afterwards, another 25 time slots are used to record the background signal without probe. Each HCPCF loading cycle is followed by a reference measurement without atoms inside the HCPCF, by keeping the MOT quadrupole field off. We therefore can detect the background due to the laser fields and due to scattered photons from the atoms inside the HCPCF independently.

Appendix C: LSR & SLP Data Acquisition & Analysis

The transmitted photons are detected by a single-photon counting module (SPCM, PerkinElmer, SPCM-

AQRH-12). The TTL output pulses of the SPCM are recorded with a digital oscilloscope (100 MHz bandwidth). The oscilloscope is triggered by the start of the first probe pulse. All events are then recorded during one measurement sequence lasting 200 μ s (corresponding to 50 measurement windows separated by 4 μ s) where the FORT is modulated for each single HCPCF loading cycle. In addition, the data is averaged over 60 HCPCF loading cycles. The temporally resolved transmission signal is then generated via software analysis by slicing the data into bins of 30 ns width and averaging over the different measurement time slots as well as different HCPCF loading cycles. The same applies to the background signal which is subtracted from the recorded data. The magnitude of the background signal for the measurements shown in Fig. 3(b) is 1.1×10^4 (0.7×10^4) photons per second with (without) atoms inside the HCPCF.

-
- [1] M. A. Nielsen and I. L. Chuang, *Quantum computation and quantum information* (Cambridge Univ. Press, 2001).
- [2] D. V. Strekalov and G. Leuchs, Nonlinear Interactions and Non-classical Light, in *Quantum Photonics: Pioneering Advances and Emerging Applications*, edited by R. W. Boyd, S. G. Lukishova, and V. N. Zadkov (Springer International Publishing, Cham, 2019) pp. 51–101.
- [3] G. Brennen, E. Giacobino, and C. Simon, Focus on Quantum Memory, *New Journal of Physics* **17**, 050201 (2015).
- [4] D. Chang, V. Vuletić, and M. Lukin, Quantum nonlinear optics — photon by photon, *Nature Photonics* **8**, 685 (2014).
- [5] Y.-F. Hsiao, P.-J. Tsai, H.-S. Chen, S.-X. Lin, C.-C. Hung, C.-H. Lee, Y.-H. Chen, Y.-F. Chen, I. A. Yu, and Y.-C. Chen, Highly efficient coherent optical memory based on electromagnetically induced transparency, *Physical Review Letters* **120**, 183602 (2016).
- [6] M. Fleischhauer, A. Imamoglu, and J. P. Marangos, Electromagnetically induced transparency: Optics in coherent media, *Reviews of Modern Physics* **77**, 633 (2005).
- [7] J. L. Everett, D. B. Higginbottom, G. T. Campbell, P. K. Lam, and B. C. Buchler, Stationary Light in Atomic Media, *Advanced Quantum Technologies* **1800100**, 1800100 (2019).
- [8] M. D. Lukin and A. Imamoglu, Controlling photons using electromagnetically induced transparency., *Nature* **413**, 273 (2001).
- [9] M. D. Lukin and A. André, Manipulating Light Pulses via Dynamically Controlled Photonic Band gap, *Physical Review Letters* **89**, 143602 (2002).
- [10] A. André, M. Bajcsy, A. S. Zibrov, and M. D. Lukin, Nonlinear Optics with Stationary Pulses of Light, *Physical Review Letters* **94**, 63902 (2005).
- [11] D. E. Chang, V. Gritsev, G. Morigi, V. Vuletić, M. D. Lukin, and E. A. Demler, Crystallization of strongly interacting photons in a nonlinear optical fibre, *Nature Physics* **4**, 884 (2008).
- [12] M. Hafezi, D. Chang, V. Gritsev, E. Demler, and M. Lukin, Quantum transport of strongly interacting photons in a one-dimensional nonlinear waveguide, *Physical Review A* **85**, 013822 (2012).
- [13] T. Chanelière, D. N. Matsukevich, S. D. Jenkins, S.-Y. Lan, T. A. B. Kennedy, and A. Kuzmich, Storage and retrieval of single photons transmitted between remote quantum memories, *Nature* **438**, 833 (2005).
- [14] Y. Wang, J. Li, S. Zhang, K. Su, Y. Zhou, K. Liao, S. Du, H. Yan, and S.-L. Zhu, Efficient quantum memory for single-photon polarization qubits, *Nature Photonics* **13**, 346 (2019).
- [15] K.-K. Park, Y.-W. Cho, Y.-T. Chough, and Y.-H. Kim, Experimental Demonstration of Quantum Stationary Light Pulses in an Atomic Ensemble, *Physical Review X* **8**, 021016 (2018).
- [16] Y.-H. Chen, M.-J. Lee, W. Hung, Y.-C. Chen, Y.-F. Chen, and I. A. Yu, Demonstration of the Interaction between Two Stopped Light Pulses, *Physical Review Letters* **108**, 173603 (2012).
- [17] A. V. Gorshkov, A. André, M. D. Lukin, and A. S. Sørensen, Photon storage in Λ -type optically dense atomic media. II. Free-space model, *Physical Review A* **76**, 033805 (2007).
- [18] S. Ghosh, A. R. Bhagwat, C. K. Renshaw, S. Goh, A. L. Gaeta, and B. J. Kirby, Low-Light-Level Optical Interactions with Rubidium Vapor in a Photonic Band-Gap Fiber, *Physical Review Letters* **97**, 023603 (2006).
- [19] T. Takekoshi and R. J. Knize, Optical Guiding of Atoms through a Hollow-Core Photonic Band-Gap Fiber, *Physical Review Letters* **98**, 210404 (2007).
- [20] M. Bajcsy, S. Hofferberth, V. Balic, T. Peyronel, M. Hafezi, A. S. Zibrov, V. Vuletić, and M. D. Lukin, Efficient All-Optical Switching Using Slow Light within a Hollow Fiber, *Physical Review Letters* **102**, 203902 (2009).
- [21] K. P. Nayak, M. Sadgrove, R. Yalla, F. L. Kien, and K. Hakuta, Nanofiber quantum photonics, *Journal of Optics* **20**, 073001 (2018).
- [22] A. Goban, C.-L. Hung, S.-P. Yu, J. Hood, J. Muniz, J. Lee, M. Martin, A. McClung, K. Choi, D. E. Chang, O. Painter, and H. J. Kimble, Atom-light interactions in photonic crystals, *Nature Communications* **5**, 3808 (2014).

- [23] M. R. Sprague, P. S. Michelberger, T. F. M. Champion, D. G. England, J. Nunn, X.-M. Jin, W. S. Kolthammer, A. Abdolvand, P. S. J. Russell, and I. A. Walmsley, Broadband single-photon-level memory in a hollow-core photonic crystal fibre, *Nature Photonics* **8**, 287 (2014).
- [24] B. Gouraud, D. Maxein, A. Nicolas, O. Morin, and J. Laurat, Demonstration of a Memory for Tightly Guided Light in an Optical Nanofiber, *Physical Review Letters* **114**, 1 (2015).
- [25] C. Sayrin, C. Clausen, B. Albrecht, P. Schneeweiss, and A. Rauschenbeutel, Storage of fiber-guided light in a nanofiber-trapped ensemble of cold atoms, *Optica* **2**, 353 (2015).
- [26] F. Blatt, T. Halfmann, and T. Peters, One-dimensional ultracold medium of extreme optical depth, *Optics Letters* **39**, 446 (2014), arXiv:1311.0635v2.
- [27] G. Bouwmans, F. Luan, J. Knight, P. St. J. Russell, L. Farr, B. Mangan, and H. Sabert, Properties of a hollow-core photonic bandgap fiber at 850 nm wavelength, *Optics Express* **11**, 1613 (2003).
- [28] M. Wegmuller, M. Legré, N. Gisin, T. Hansen, C. Jakobsen, and J. Broeng, Experimental investigation of the polarization properties of a hollow core photonic bandgap fiber for 1550 nm, *Optics Express* **13**, 1457 (2005).
- [29] F. Poletti, N. G. R. Broderick, D. J. Richardson, and T. M. Monro, The effect of core asymmetries on the polarization properties of hollow core photonic bandgap fibers, *Optics Express* **13**, 9115 (2005).
- [30] M. Fleischhauer and M. D. Lukin, Quantum memory for photons: Dark-state polaritons, *Physical Review A* **65**, 22314 (2002).
- [31] F. Blatt, L. S. Simeonov, T. Halfmann, and T. Peters, Stationary light pulses and narrowband light storage in a laser-cooled ensemble loaded into a hollow-core fiber, *Physical Review A* **94**, 043833 (2016).
- [32] G. Genov, T. E. Lellinger, T. Halfmann, and T. Peters, Laser frequency stabilization by bichromatic saturation absorption spectroscopy, *Journal of the Optical Society of America B* **34**, 2018 (2017).
- [33] M. Fleischhauer and M. D. Lukin, Dark-State Polaritons in Electromagnetically Induced Transparency, *Physical Review Letters* **84**, 5094 (2000).
- [34] M. Bajcsy, A. S. Zibrov, and M. D. Lukin, Stationary pulses of light in an atomic medium., *Nature* **426**, 638 (2003).
- [35] F. E. Zimmer, A. André, M. D. Lukin, and M. Fleischhauer, Coherent control of stationary light pulses, *Optics Communications* **264**, 441 (2006).
- [36] Y.-W. Lin, W.-T. Liao, T. Peters, H.-C. Chou, J.-S. Wang, H.-W. Cho, P.-C. Kuan, and I. A. Yu, Stationary Light Pulses in Cold Atomic Media and without Bragg Gratings, *Physical Review Letters* **102**, 213601 (2009).
- [37] C. L. Chen, *Found. Guid. Opt.* (John Wiley & Sons, Inc., 2005) pp. 1–462.
- [38] W. J. Tabor and F. S. Chen, Electromagnetic Propagation through Materials Possessing Both Faraday Rotation and Birefringence: Experiments with Ytterbium Orthoferrite, *J. Appl. Phys.* **40**, 2760 (1969).
- [39] K. Kikuchi and T. Okoshi, Wavelength-sweeping technique for measuring the beat length of linearly birefringent optical fibers., *Optics letters* **8**, 122 (1983).